Benchmarking Rod–Airfoil Aeroacoustics Using Higher-Order Flux-Reconstruction Scheme

Rishit B. Modi,* Mohammad Alhawwary,† Freddie D. Witherden,‡ and Antony Jameson§
Texas A&M University, College Station, Texas 77840

https://doi.org/10.2514/1.J066222

An implicit large-eddy simulation (ILES) is performed on the rod–airfoil benchmark case coupled with a time-domain Ffowcs Williams–Hawkings acoustic analogy formulation to predict aeroacoustic noise. The compressible Navier–Stokes equations are solved using the high-order solver PyFR, an open-source framework for solving advection-diffusion problems using high-order flux reconstruction schemes. Reynolds number based on the airfoil chord length is 480,000, and the Mach number M is 0.21. This study evaluates the applicability and accuracy of high-order flux reconstruction in an ILES framework for computational aeroacoustics focusing on both aerodynamics and acoustic predictions. PyFR simulations predict the dominant tonal frequency at a Strouhal number of 0.18. The far-field acoustic spectra show good agreement with the published literature. The influence of spanwise resolution domain length is quantified, demonstrating that spanwise resolution has a modest effect on the near-field aerodynamics and far- field acoustics, whereas the spanwise domain length has a substantially stronger impact. The individual noise contributions from the rod and airfoil are analyzed and reveal that the airfoil dominates the overall noise except at very high frequencies. Constructive interference between the two sources leads to elevated overall sound pressure levels. Directivity analysis confirms that the radiated sound field exhibits a predominantly dipolar pattern.

Nomenclature

C	=	airfoil chord, m
C_d	=	drag coefficient
C_f	=	skin friction coefficient
C_L	=	lift coefficient
C_p	=	pressure coefficient
c	=	speed of sound, m/s
c_p	=	specific heat at constant pressure, J/(kg · K)
c_v	=	specific heat at constant volume, J/(kg · K)
D	=	cylinder diameter, m
d	=	rod diameter, m
E	=	energy, J
$\boldsymbol{f}^i$	=	inviscid flux
$\boldsymbol{f}^v$	=	viscous flux
L	=	loading noise, kg/(m · s^2)
Lt	=	Ffowcs Williams–Hawkings window length
M	=	Mach number
$\wp$	=	polynomial order
Pr	=	Prandtl number
p	=	pressure, Pa
p_0	=	undisturbed pressure, Pa
p'	=	perturbed pressure, Pa
Q	=	thickness source term, kg/(m^2 · s)
q	=	heat flux, W/m^2
R	=	acoustic radius, m
R^*	=	amplitude radius, m
R_e	=	Reynolds number
$\tilde{R}_i$	=	gradient of acoustic radius
St	=	Strouhal number
T	=	temperature, K
t	=	physical time, s
$\tilde{t}$	=	nondimensional time
U_∞	=	freestream velocity, m/s
γ	=	ratio of specific heats
μ	=	dynamic viscosity, Pa · s (Pascal-second)
ρ	=	density, kg/m^3
ρ_0	=	undisturbed density, kg/m^3
ρ'	=	perturbed density, kg/m^3
τ	=	shear stress, Pa

Superscripts

$+$	=	wall nondimensional units
∞	=	freestream quantity

Subscript

n	=	surface normal component

I. Introduction

THE push toward green aviation has intensified global efforts to reduce not only carbon emissions but also various forms of aircraft community noise. Among these, airframe, landing gear, and jet noise have received considerable attention due to their significant impact on both military and civilian populations, particularly in urban areas where airports are often located near high-density residential zones. The push for lower aircraft noise is intensified by the recent recommendation for a new Chapter 16 noise standard by International Civil Aviation Organization. The new standards would require an additional 6 dB reduction beyond Chapter 14 for new subsonic aircraft starting in January 2029 [1]. Meeting such stringent requirements through experimental testing alone is prohibitively expensive and time consuming, particularly during the early stages of aircraft design. As a result, predictive aeroacoustic tools capable of accurately capturing noise generation are essential for guiding noise reduction strategies.

Among existing computational methods for predicting sound propagation in fluid media, the hybrid large-eddy simulation (LES–)acoustic analogy approach has emerged as a practical and widely used framework in computational aeroacoustics. In this approach, the Navier–Stokes equations are solved to resolve the near-field turbulent flow structures, which are then used as input in acoustic analogy formulations to compute far-field sound propagation. The accuracy of far-field

Presented as Paper 2023-0978 at the AIAA Scitech 2023, National Harbour, MD, January 23–27, 2023; received 11 August 2025; accepted for publication 11 February 2026; published online 29 April 2026.

*Ph.D. Student, Department of Ocean Engineering; rishit@tamu.edu (Corresponding Author).

†Postdoctoral Researcher, currently Lead Engineer, GE Aerospace; mohammadalhawwary@gmail.com.

‡Associate Professor, Department of Ocean Engineering; fdw@tamu.edu.

§Professor, Department of Aerospace Engineering; antony.jameson@tamu.edu.

noise predictions is therefore strongly dependent on the fidelity of the near-field turbulence solution. LES provides a favorable balance between accuracy and computational cost by explicitly resolving the dominant energy-containing eddies while modeling only the smaller, more dissipative scales. As a result, this hybrid approach has been widely applied to jet noise prediction and other turbulent flow-induced noise problems.

Several researchers have employed the hybrid approach for jet noise predictions [2–6] as well as other turbulent flow-based noise predictions [7–10]. Casalino et al. [7] did a 2D unsteady RANS (URANS) simulation combined with a statistical model to account for the 3D spanwise effect. URANS was unable to capture the broadband spectrum of the wall-pressure spectrum and resulted in a significant overprediction of the shedding frequency. Boudet et al. [11] performed LES simulations of the rod–airfoil configuration on a mesh with 2.4 million cells. Their z^+ is 350, resulting in low spanwise resolution compared to wall flow scales ($y^+ < 1.25$). They correctly capture the near-field aerodynamics, but their far-field acoustics overestimate the high-frequency content. Eltaweel and Wang [12] use an incompressible boundary-element LES approach combined with Lighthill's equation to obtain the acoustic radiation. The far-field acoustics show slightly broader and lower peaks possibly due to aliasing caused by insufficient sampling time. They demonstrate good overall agreement of the near-field and far-field acoustics with existing literature. Berland [13] used an overset grid to carry out compressible LES simulations of the rod–airfoil setup. They used 20 million cells with a y^+ of less than 3. The far-field acoustic results show a significant overprediction in the low-frequency range, while an underprediction is observed in the high frequency range. Peth et al. [14] calculated the flowfield using an implicit LES incompressible solver. The acoustic computations were done by solving a linearized version of the compressible Navier–Stokes, and a y^+ of 10 was used for this study.

Although rod–airfoil noise has been extensively studied using LES, RANS, and other numerical frameworks, these approaches have not fully exploited the potential of modern high-order methods tailored for unstructured grids. Conventional low-order finite-volume schemes, while robust, often introduce excessive numerical dissipation and dispersion. Because aeroacoustic phenomena are governed by small-amplitude pressure fluctuations propagating over long distances, excessive numerical dissipation or dispersion can contaminate acoustic predictions. High-order numerical methods offer significant advantages for aeroacoustic simulations due to their superior dispersion and dissipation properties compared to low-order schemes [15]. Discontinuous spectral element methods (DSEMs) have gained attraction for LES due to their ability to achieve high-order spatial accuracy in unstructured grids and a compact stencil that is suited for massively parallel computations. Some of the popular DSEM methods include the nodal discontinuous Galerkin method [16] and the flux reconstruction (FR) method of Huynh [17]. Vincent et al. [15] have shown that flux reconstruction scheme has increased numerical dissipation at high frequencies, enabling it to function effectively as an implicit large-eddy simulation (ILES) method. This inherent dissipation allows the simulation of turbulent flows without the need for an explicit subgrid-scale (SGS) model. By avoiding such models, ILES eliminates the computational overhead and parameter tuning typically associated with traditional LES approaches. In addition, these methods can work routinely with mixed unstructured grids, which is needed for complex geometries involved in airplane noise problems. DSEMs have recently been employed with considerable success for jet noise prediction [18,19], demonstrating the potential of high-order schemes in aeroacoustic applications.

Building on these developments, the purpose of the present study is to investigate the FR method and evaluate the effectiveness of ILES for rod–airfoil noise prediction. To the best of our knowledge, this work represents the first application of the FR method combined with ILES to the canonical rod–airfoil problem. Indeed, this problem contains many of the interesting noise features encountered in a landing-gear problem such as the quasi-tonal noise caused by the vortex shedding of the rod and broadband noise spectrum due to impingement of the rod wake on the airfoil surface. The availability of extensive experimental and numerical data makes it an ideal test case for evaluating numerical methods for bluff-body-induced noise in turbulent separated flows [20].

The standard setup consists of a turbulent flow simulation over a rod placed 1.05C in front of NACA0012 airfoil at 0 deg angle of attack at $Re = 480{,}000$ and $M = 0.21$ from the experiment of Jacob et al. [21]. In this work, we augmented the high-order cross-platform solver PyFR [22] with a Ffowcs Williams–Hawkings (FWH) solver implemented in Python for the simulation of the rod–airfoil turbulent-flow-based noise prediction problem. We analyze the effectiveness of higher-order flux reconstruction method combined with ILES for aeroacoustic noise predictions. The influence of the spanwise domain length as well as spanwise mesh resolution on the near-field aerodynamics and far-field acoustics is analyzed. We benchmark the near-field aerodynamic quantities pressure coefficient C_p, drag coefficient C_D, and lift coefficient C_L against the experimental and numerical studies in the literature. Far-field acoustic predictions are computed and validated against published results. In addition, the individual noise contributions from the rod and the airfoil are analyzed, and the acoustic directivity of the rod–airfoil configuration is investigated. This paper is organized as follows. Section II is dedicated for introducing the numerical models where both the flow and acoustic solvers are discussed. We then present the problem setup in Sec. III and the numerical results in Sec. IV.

II. Methodology

A. FR Method and PyFR Solver

The flow model is based on the compressible Navier–Stokes equations, which can be written in a conservative form as

$$\frac{\partial \boldsymbol{U}}{\partial t} + \nabla \cdot \boldsymbol{f} = 0 \tag{1}$$

where $\boldsymbol{U}(\boldsymbol{x}, t) = (\rho, \rho u_x, \rho u_y, \rho u_z, E)$ is the solution; ρ is the density; $\boldsymbol{u} = (u_x, u_y, u_z)$ are the fluid velocity components in x, y, z directions, respectively; and E is the total energy per volume of the fluid. Here, $\boldsymbol{f} = \boldsymbol{f}(\boldsymbol{u}, \nabla \boldsymbol{u}) = \boldsymbol{f}^i - \boldsymbol{f}^v$ is the flux with $\boldsymbol{f}^i$ being the inviscid flux given by

$$\boldsymbol{f}^i_{lm} = \begin{pmatrix} \rho u_m \\ \rho u_l u_m + p\delta_{lm} \\ u_m(E + p) \end{pmatrix} \tag{2}$$

where p is given by

$$p = (\gamma - 1)\left(E - \frac{1}{2}\rho \|\boldsymbol{u}\|^2\right) \tag{3}$$

where $\gamma = c_p/c_v$, where c_p and c_v are specific heat capacities at constant pressure and volume, respectively. The viscous flux is

$$\boldsymbol{f}^v_{lm} = \begin{pmatrix} 0 \\ \tau_{lm} \\ u_l \tau_{lm} - q_m \end{pmatrix} \tag{4}$$

The components of the stress–energy tensor are given by

$$\tau_{lm} = \mu(\partial_l u_m + \partial_m u_l) - \frac{2}{3}\mu\delta_{lm}\nabla \cdot \boldsymbol{u} \tag{5}$$

The heat flux q_m is given by

$$q_m = -k\frac{\partial T}{\partial x_m} \tag{6}$$

Using the ideal gas law, the temperature is

$$T = \frac{1}{c_v}\frac{1}{\gamma - 1}\frac{p}{\rho} \tag{7}$$

In this study, the compressible Navier–Stokes equations are solved with a multidimensional FR approach for space discretization implemented in PyFR. PyFR is an open-source software that can solve the compressible Navier–Stokes equations on mixed unstructured grids and is designed to target a range of modern hardware platforms, including heterogeneous mixtures of CPUs and Graphics Processing Units (GPUs), via C/OpenMP, CUDA, HIP, and OpenCL backends [22,23]. PyFR exploits distributed memory parallelism by dividing the computational domain across multiple GPUs using a message passing interface (MPI), while within each GPU, thousands of cores handle fine-grained parallelism. The FR approach introduced by Huynh [24] is a nodal numerical formulations for solving hyperbolic partial differential equations. The method has been further developed by several groups [25–27] for advection–diffusion problems and extended to mixed unstructured grids [23,28]. In addition, high-order FR method has proved successful for a number of large-eddy simulations based on the implicit approach [29] as shown in Refs. [30–33] and more recently based on the partially averaged Navier–Stokes equations in Ref. [34].

In the FR method, the domain Ω is partitioned into N_e non-overlapping elements Ω_e such that $\bigcup_{i=1}^{N_e} \Omega_e = \Omega$. Considering Eq. (1), the solution vector takes the form

$$\boldsymbol{u} = \sum_{i=1}^{N_p} \boldsymbol{u}_i \phi_i \tag{8}$$

inside each element Ω_e. Here, N_p is the number of solution points inside the element, and ϕ is the set of nodal basis functions. A discontinuous approximation of the flux is obtained by taking a collocation projection of the flux function on the solution nodes and is defined as

$$\boldsymbol{f}^D = \sum_{i=1}^{N_p} \boldsymbol{f}_i^D \phi_i \tag{9}$$

where $\boldsymbol{f}_i^D$ is the value of the flux at solution points. To allow for data interaction between adjacent cells in flux reconstruction, the discontinuous flux $\boldsymbol{f}^D$ is corrected by adding a correction flux polynomial. After adding the correction, the flux function takes the form

$$\boldsymbol{f}^C = \boldsymbol{f}^D + \sum_{i=1}^{N_f} [(\boldsymbol{f}\cdot\boldsymbol{n})_i^I - (\boldsymbol{f}^D\cdot\boldsymbol{n})_i]\boldsymbol{h}_i \tag{10}$$

where $(\boldsymbol{f}\cdot\boldsymbol{n})_i^I$ is the normal component of the flux computed at interface flux point i. N_f is the number of flux points, $\boldsymbol{n}$ represent the normal vectors at the flux points, and $\boldsymbol{h}_i$ is the correction function, which belongs to the Raviart–Thomas space. The corrected flux $\boldsymbol{f}^C$ can now be differentiated to obtain the divergence of flux. At each element interface, the solution is discontinuous resulting in two distinct states at the interface. The flux is evaluated using these solution values and is supplied to a Riemann solver, which returns a single conservative numerical flux that is used as the common interface flux $(\boldsymbol{f}\cdot\boldsymbol{n})_i^I$ for both elements. In the present work, a Rusanov Riemann solver [35] using the Davis wave speed [36] is used to calculate the interelement inviscid fluxes. The local discontinuous Galerkin [37] approach is used to calculate the interelement viscous fluxes combined with an adaptive time-step Runge–Kutta scheme [38] to advance the solution in time. For more details on the FR method, interested readers can consult the following reviews [39,40]. A key benefit of the FR method is its compact, element-local stencil, which minimizes memory indirection on unstructured grids and preserves spatial locality leading to improved cache efficiency and superior performance on modern CPU and GPU architectures. The locally compact stencil of the FR method significantly reduces internode MPI communication by restricting coupling to a small set of neighboring elements. FR scheme offers geometric flexibility by supporting unstructured grids composed of mixed elements (hexahedra, prisms, and tetrahedra), which allows for the high-order resolution of complex aerodynamic features such as boundary layers and wake interactions without the constraints of structured meshes. Spectral resolution is achieved using FR scheme, resulting in significantly lower dissipation and dispersion compared to traditional finite volume schemes. The mathematical structure of the flux reconstruction scheme naturally enables PyFR to overlap communication with computation in multi-GPU environments. Majority of the operations within an FR step can be cast as matrix–matrix multiplications, and PyFR exploits this property by leveraging highly optimized vendor Basic Linear Algebra Subprograms (BLAS) libraries, such as cuBLAS and rocBLAS for dense matrix–matrix operations, while sparse matrix–matrix multiplications are handled using the GiMMiK library [41] tailored specifically for the FR operator structure. To further enhance performance, PyFR adopts a task-graph execution model for GPU kernels, allowing independent computational tasks to be scheduled asynchronously. Further details regarding the implementation and performance optimizations are provided in Ref. [42].

B. FWH Solver

The *permeable/porous* surface FWH equations based on the moving medium formulation [43] can be written using index summation notation as

$$\Box^2[H(f)p'(x,t)] = \frac{D}{Dt}[Q\delta(f)] - \frac{\partial}{\partial x_l}[L_l\delta(f)] \tag{11}$$

where $\Box^2 = (1/c^2)(D^2/Dt^2) - (\partial^2/\partial x_i \partial x_i)$ is the d'Alembert wave operator and

$$\begin{aligned} L_l &= \rho u_l[u_n - (v_n - U_{\infty n})] + [(p - p_0)\delta_{lm} - \sigma_{lm}]\hat{n}_m, \\ Q &= \rho[u_n - (v_n - U_{\infty n})] + \rho_0(v_n - U_{\infty n}) \end{aligned} \tag{12}$$

In the present work, the quadrupole volume source term in the Ffowcs Williams–Hawkings formulation is neglected. The description of the given symbols is as follows. On the left-hand side of Eq. (11), $p' = p - p_\infty$ is the acoustic perturbation pressure. For small disturbances $\rho'/\rho_\infty \ll 1$, the pressure disturbance/acoustic pressure $p' = c^2\rho' = c^2(\rho - \rho_\infty)$ is valid for the left-hand side of the equation, which is evaluated for an observer distance far away from the surface where the flow can be assumed isentropic. The symbols p_∞, ρ_∞ are the pressure and density of the undisturbed flow and c is the speed of sound, that is, freestream values. $H(f)$ is the Heaviside function which is defined as

$$H(f(\boldsymbol{x},t)) = \begin{cases} 1: & f(\boldsymbol{x},t) > 0 \\ 0: & f(\boldsymbol{x},t) < 0 \end{cases} \tag{13}$$

and $\delta(f)$ is the Dirac delta function defined as

$$\delta(f(\boldsymbol{x},t)) = \frac{\partial H}{\partial f} = \begin{cases} 1: & f(\boldsymbol{x},t) = 0 \\ 0: & f(\boldsymbol{x},t) \neq 0 \end{cases} \tag{14}$$

and $f(\boldsymbol{x},t)$ is the data surface equation as shown in Fig. 1a.

Q and L represent the thickness and loading source terms and are surface distribution of sources, u_n is the normal component of the perturbed fluid velocity, and v_n is the normal surface velocity assuming a fixed frame of reference x. This completes the presentation of the FWH equation for stationary observer in a moving medium. In the present work, we neglect the viscous stress effects σ_{lm}. Note that for a stationary permeable FWH surface Eq. (11) still applies with $v_n = 0$ to satisfy the zero surface velocity condition.

For a stationary permeable data surface, following Ref. [43], the acoustic pressure in the time domain can be computed as

$$p(\boldsymbol{x},t,\boldsymbol{M}_\infty) = p_L(\boldsymbol{x},t,\boldsymbol{M}_\infty) + p_T(\boldsymbol{x},t,\boldsymbol{M}_\infty) \tag{15}$$

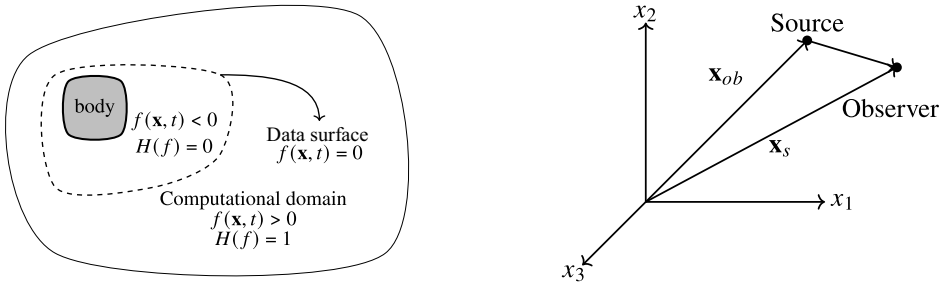

a) Computational domain **b) Frames of reference**

Fig. 1 Acoustics model.

where $\boldsymbol{M}_\infty$ is the freestream Mach number vector; p_L and p_T are the loading and thickness pressure contributions given by

$$4\pi p_L = \frac{1}{c_\infty}\int_S \frac{\dot{L}_i \tilde{R}_i}{R^*}\,\mathrm{d}S + \int_S \frac{L_i \tilde{R}_i^*}{R^{*2}}\,\mathrm{d}S,$$
$$4\pi p_T = \int_S \frac{(1 - M_{\infty,i}\tilde{R}_i)\dot{Q}}{R^*}\,\mathrm{d}S - \int_S \frac{Q c_\infty M_{\infty,i}\tilde{R}_i^*}{R^{*2}} \tag{16}$$

The amplitude radius R^* and the phase radius R are given by

$$R^* = \frac{1}{\gamma}\sqrt{r^2 + \gamma^2 M_{\infty r}^2}, \qquad R = \gamma^2(R^* - rM_{\infty r}) \tag{17}$$

where $r = |\boldsymbol{x} - \boldsymbol{y}(\tau)|$ is the distance between the source position $\boldsymbol{x}_s$ and the observer position $\boldsymbol{y}$; see Fig. 1b. In addition, $M_{\infty r} = M_{\infty i} r_i$ and $\gamma = 1/\sqrt{1 - |M_\infty^2|}$. The terms $\dot{L}$ and $\dot{Q}$ represent the time derivatives of L and Q, respectively. The quantities $\tilde{R}^*$ and $\tilde{R}$ are the gradients of amplitude and phase radius and are given by

$$\tilde{R}_i^* = \frac{r_i + \gamma^2(M_{\infty j} r_j)}{\gamma^2 R^*}, \qquad \tilde{R}_i = \gamma^2(\tilde{R}^* - rM_{\infty r}) \tag{18}$$

Equation (16) is solved in time domain in an online manner to obtain the acoustics. PyFR routinely works with unstructured grids, and the extraction of the acoustic data surface is done based on actual face elements. In PyFR, the FWH solver is implemented as an acoustic plugin feature, which periodically samples the flow solution on the specified integration surface. The computational cost of the plugin increases linearly with the number of sampling points. For the present study, the number of observers is moderate, and the additional runtime overhead associated with FWH sampling was measured to be approximately 0.6% of the total simulation time. This approach is therefore efficient for a limited number of observer locations. For applications requiring reconstruction of the acoustic field at a very large number of points, an offline postprocessing strategy based on stored FWH surface data would be more appropriate. Geometric quantities such as the acoustic radii R and R^* are computed directly by the flow solver and are made available to the plugin. Using these, the thickness and loading contributions Q and L_i are evaluated based on the instantaneous flowfield. The surface integrals in Eq. (16) are computed using numerical quadrature and the resulting acoustic pressure p is written out to a file periodically. After the simulation concludes, the time-domain acoustic signal is postprocessed in the frequency domain using Welch's method of periodograms [44]. The recorded signal over the total simulation time is divided into overlapping windows of length Lt, and each window is multiplied with an appropriate window function to reduce spectral leakage. The Fourier Transform is then computed for each window, and the resulting spectra are averaged to obtain a converged estimate of the frequency-domain acoustic pressure. The current implementation of the FWH acoustic model in PyFR is validated using a flow past a cylinder test case. Details regarding the setup, mesh parameters, and results of this validation can be found in Appendix A.

III. Problem Setup

The rod–airfoil case setup shown in Fig. 2 follows the setup of the experiment carried out by Jacob et al. [21] and the numerical simulations in the literature [20,45–48]. In this case, a rod with a diameter $d = 0.1C$ is used, and its center is placed at a distance of $1.05C$ in front of a NACA0012 airfoil at zero angle of attack, where C is the airfoil chord length. The Reynolds number ($Re = U_\infty C/\nu$) is 480,000 based on the airfoil chord. The freestream Mach number M is defined as u_∞/c and has a value of 0.21. The Prandtl number is $Pr = \mu c_p/k = 0.71$.

The simulations are carried out on three different meshes, with variations introduced primarily in the spanwise direction. Most LES studies in the literature [12,47] consider a spanwise extent of $3.5d$, whereas the spanwise coherence length at the dominant shedding frequency has been shown by Ref. [21] to be $6.5d$. To investigate the influence of the spanwise domain size on solution accuracy, meshes with different spanwise lengths are therefore considered. All meshes are generated by extruding a two-dimensional grid in the spanwise direction. Two distinct spanwise resolutions are employed to assess the effect of z^+ on the flow field. Each mesh includes a structured boundary-layer region around both the airfoil and the cylinder, with first-cell height of $3 \times 10^{-4}C$ over the airfoil and $2 \times 10^{-4}C$ over the cylinder. The near-wake region surrounding the airfoil and rod is also refined and extends downstream up to approximately $6C \sim 7C$ to ensure accurate prediction of wake turbulence. The far-field boundary has a radius of approximately $10.5C$ and is centered at $1.5C$ distance downstream of the airfoil. Figure 3 shows the front view of the mesh used for the rod–airfoil simulation. The key parameters of the three meshes are summarized in Table 1. Meshes A and C have the same resolution in the spanwise direction, but different spanwise length. Meshes A and B have the same spanwise length, but different resolution in the spanwise direction. We rely on $\wp$-convergence to assess the numerical accuracy within each element and confirm that the boundary-layer and wake physics are sufficiently resolved at a given polynomial order. Comparing results obtained using meshes A and B isolate the effect of z^+ on the flowfield, while comparing meshes A and C is used to identify the necessary spanwise length to accurately resolve the 3D vortical structures. A characteristic Riemann invariants far-field boundary condition is used to minimize wave reflections, and a no-slip adiabatic wall condition is used at rod and airfoil surface. Periodic boundary conditions are used in the spanwise direction.

Figure 4 shows the distribution of y^+ at the first solution point from the wall along both the rod and airfoil surfaces for polynomial orders $\wp = 2$ and $\wp = 3$. Because all three meshes have the same structured mesh in boundary layer, we compare the y^+ exclusively for mesh B. The y^+ is obtained using the location of the first degree

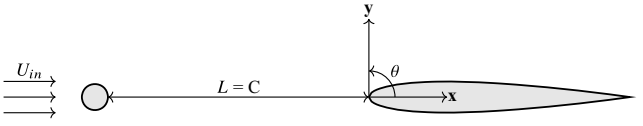

Fig. 2 Setup for the rod–airfoil problem.

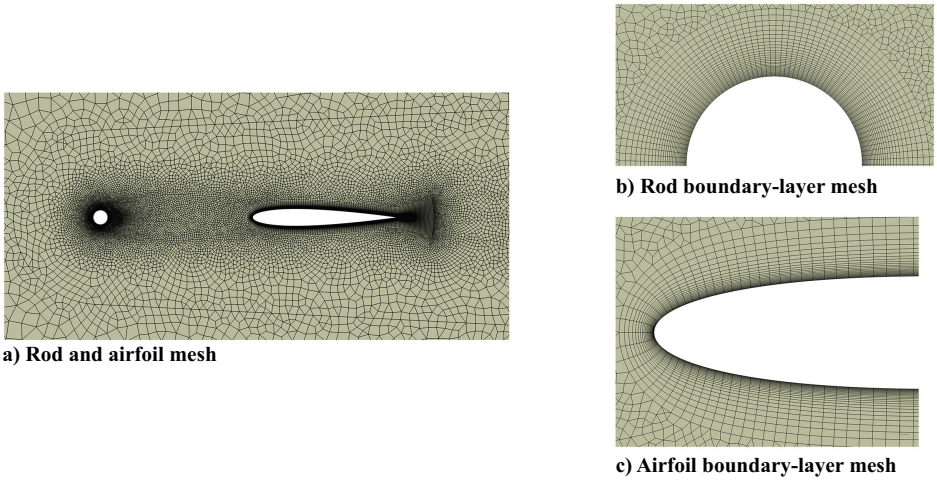

a) Rod and airfoil mesh

b) Rod boundary-layer mesh

c) Airfoil boundary-layer mesh

Fig. 3 Mesh for the rod–airfoil simulation.

Table 1 Summary of the unstructured meshes used in this study

Mesh	Spanwise length L_z, d	Spanwise points n_z	Number of elements, million
A	3.5	56	1.7
B	3.5	112	3.4
C	7	112	3.4

of freedom nearest to the wall. In general, PyFR simulation with $\wp = 3$ gives lower y^+ values for both rod and airfoil. Figure 4a shows the variation of y^+ over the rod from $\theta = 0$ deg to $\theta = 360$ deg. For $\wp = 2$, y^+ remains below 1.5, while for $\wp = 3$, it remains below 1. At $\theta = 120$ deg, the value of y^+ for $\wp = 3$ falls below $\wp = 2$. This can be attributed to the higher numerical dissipation of the $\wp = 2$ scheme. In the separation region, y^+ is consistently lower than 1 for both $\wp = 2$ and $\wp = 3$. Figure 4b shows the variation of y^+ over the airfoil in the streamwise direction. A peak value of $y^+ = 0.75$ is achieved for $\wp = 3$, and 1.3 is achieved for $\wp = 2$. We can also notice that $\wp = 3$ results in lower values for y^+ across the whole airfoil surface due to its increased resolution. Figure 5 shows the distribution of z^+ over the rod and airfoil surface for PyFR meshes A and B. Over the rod, z^+ for mesh A remains below 16, while that of mesh B remains below 10. Along the airfoil, mesh B consistently achieves $z^+ < 5$

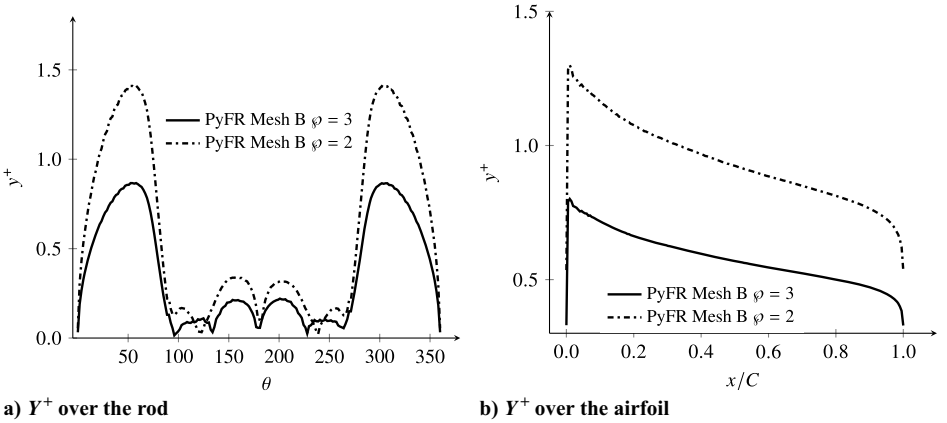

a) Y^+ over the rod

b) Y^+ over the airfoil

Fig. 4 Y^+ distribution.

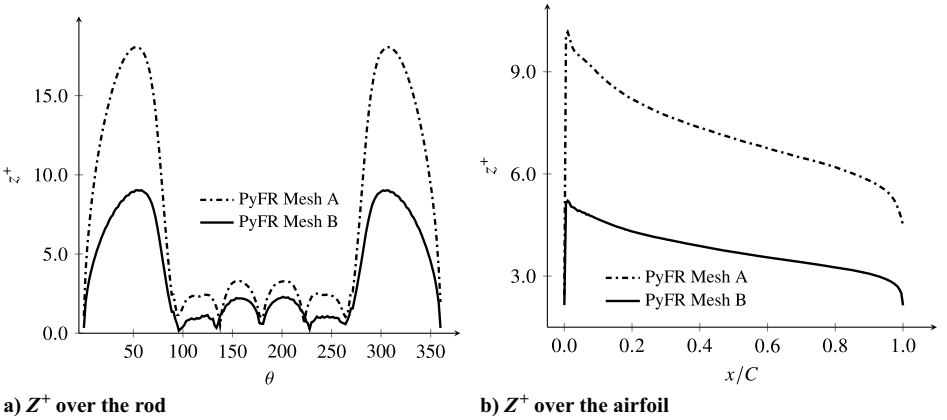

a) Z^+ over the rod

b) Z^+ over the airfoil

Fig. 5 Z^+ distribution.

across most of the chord, whereas mesh A shows substantially larger values, highlighting the improved resolution of mesh B in the spanwise direction.

IV. Numerical Results

A parallel numerical simulation on a multi-GPU architecture is conducted using PyFR in an ILES approach where no subgrid-scale modeling is used. The simulations are performed on a high-performance computing cluster using 72 V100 GPUs. Each V100 GPU is equipped with 5120 CUDA cores and 640 Tensor Cores, providing a peak double-precision performance of approximately 7.8 TFLOPS (Tera Floating Point Operations per second) (double-precision) and a memory bandwidth of 900 GB/s. NVIDIA NVLink 2.0 handles high speed intranode communication, while Mellanox EDR InfiniBand facilitated internode synchronization. Meshes A, B, and C are partitioned into 72 subdomains using METIS partitioner [49]. To ensure numerical stability during the initial transient, the simulations are run at $\wp = 2$ for a duration of 72 nondimensional time units $\tilde{t}$, with $\tilde{t}$ defined as tU_∞/C. After this startup phase, the simulations are restarted with $\wp = 3$. Averaged statistics are collected for a total duration of $\tilde{t} = 100$ units, with data accumulated every 500 physical time steps.

A. Turbulent Flow and Aerodynamic Coefficients Results

The mean and rms of the drag coefficient are presented in Table 2 for all three meshes A, B, and C. Mesh A, which serves as the baseline configuration yields a mean drag coefficient $\langle C_d \rangle = 1.39$ at $\wp = 2$, which increases marginally to 1.40 when order is raised to 3. The rms drag fluctuations and Strouhal number based on rod diameter (fD/U_∞) remain unchanged, indicating that the solution is only weakly sensitive to polynomial order for this configuration. A comparison across spanwise resolution and domain length shows minimal sensitivity of the integral quantities. Increasing the spanwise resolution from 56 to 112 points at fixed domain length does not alter the mean or rms drag, suggesting that mesh A already provides adequate spanwise resolution. Doubling the spanwise extent to $L_z = 0.7$ while maintaining 112 points (mesh C) results in a slight reduction of the mean drag to $\langle C_d \rangle = 1.37$, while the rms drag and Strouhal number remain unchanged. This indicates a weak influence of spanwise domain length on the mean drag. The rms value of drag coefficient $C_{d,\mathrm{rms}}$ is 25% lower than that of the experiment but matches closely with the LES results of Ref. [47]. Overall, the PyFR results show good agreement with the experimental measurements of Ref. [50] with discrepancies in $\langle C_d \rangle < 3\%$. The discrepancy between the present high-order ILES and the reference LES is likely attributed to the numerical dissipation inherent in the different schemes. The high-order FR approach has lower dissipation, allowing it to resolve finer turbulent structures in the shear layer and near wake. In lower-order methods or simulations with explicit SGS models, excessive numerical viscosity can dampen shear-layer instabilities resulting in lower mean drag. The close agreement between the present results and experimental data suggests that the ILES approach correctly captures the wake dynamics without the need for explicit turbulence modeling. The predicted Strouhal number St is 0.18 for all simulated cases, which is slightly lower than the experimental value reported by Ref. [50] and LES results of Ref. [47]. This systematic underprediction of the shedding frequency is largely insensitive to spanwise resolution, domain length, and polynomial order, suggesting that it is not driven by numerical resolution effects. Overall, the ILES–PyFR simulations provide consistent predictions of the mean and rms drag coefficients across all meshes considered while exhibiting a slight underprediction of vortex shedding frequency. Figure 6 shows the time-averaged velocity field in the wake of the rod and airfoil. The rod wake exhibits periodic vortex shedding, while the airfoil wake is characterized by smaller, less coherent turbulent eddies. Points P1–P6 highlighted in Fig. 6 are used to analyze pressure and velocity signals in the rod and airfoil wake. Figure 7 shows the instantaneous vortical structures of the rod–airfoil configuration visualized using isosurfaces of the Q-criterion, colored by velocity magnitude. The visualization highlights the breakdown of the cylinder wake and the interaction of turbulent eddies with the airfoil leading edge, identifying the primary sources of broadband noise generation. Figure 8 represents the power spectral density (PSD) of drag and lift coefficient over the cylinder plotted against Strouhal number for three PyFR meshes. All three meshes exhibit similar variation of the lift and drag coefficients. Mesh C has a slightly higher drag coefficient at low frequencies ($St < 0.05$). The lift coefficient has the fundamental shedding frequency of 0.18 for all three meshes. The peak frequency of drag coefficient is 0.36 and corresponds to the first harmonic, which is twice that of the fundamental shedding frequency. This is consistent with the results of Refs. [51,52] that lift fluctuations occur at the fundamental shedding frequency, while drag fluctuations dominate at twice that frequency. The lift coefficient also shows a prominent peak corresponding to the second harmonic at $St = 0.54$.

Figure 9a shows the variation of the mean pressure coefficient $\langle C_p \rangle$ over the cylinder for PyFR simulations for the three meshes A, B, and C. Additionally, mesh B results are shown for two polynomial orders $\wp = 2$ and $\wp = 3$. These results are compared with the LES data of Giret et al. [47] and the experimental measurements of Ref. [50] on an isolated rod. All PyFR simulations exhibit consistent results, converging to nearly identical C_p distributions, indicating mesh and order independence. C_p attains a value of 1 at the forward stagnation point and decreases steadily up to $\theta = 70$ deg. The pressure coefficient increases from $\theta = 70$ deg to $\theta = 93$ deg, beyond which it starts to decrease. This reversal in the pressure gradient indicates the onset of boundary-layer separation at $\theta = 93$ deg. The pressure coefficient reaches its minima at $\theta = 180$ deg, and the minimum value (−1.5) matches exactly

Table 2 Mean and rms drag coefficients for the rod

Cases	$\langle C_d \rangle$	$C_{d,\mathrm{rms}}$	St
ILES PyFR Mesh A ($Re = 4.8 \times 10^4$), $\wp$	1.39	0.12	0.18
ILES PyFR Mesh A ($Re = 4.8 \times 10^4$), $\wp = 3$	1.4	0.12	0.18
ILES PyFR Mesh B ($Re = 4.8 \times 10^4$), $\wp = 3$	1.4	0.12	0.18
ILES PyFR Mesh C ($Re = 4.8 \times 10^4$), $\wp = 3$	1.37	0.12	0.18
Experiment Szepessy ($Re = 4.3 \times 10^4$) [50]	1.35	0.15	0.19
LES Giret et al. ($Re = 4.8 \times 10^4$) [47]	1.19	0.12	0.19

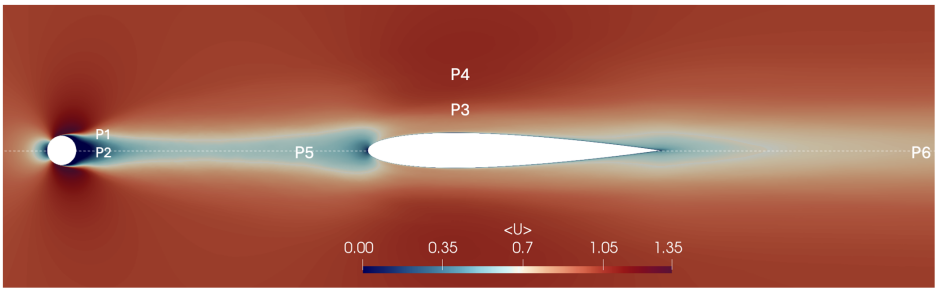

Fig. 6 Time-averaged streamwise velocity component for flow over rod–airfoil configuration.

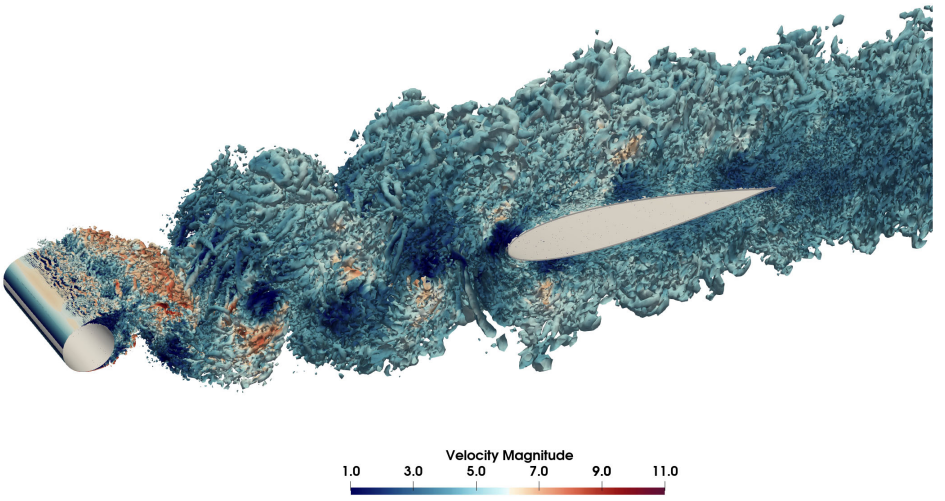

Fig. 7 Q-criterion at $\tilde{t} = 150$ colored by velocity magnitude.

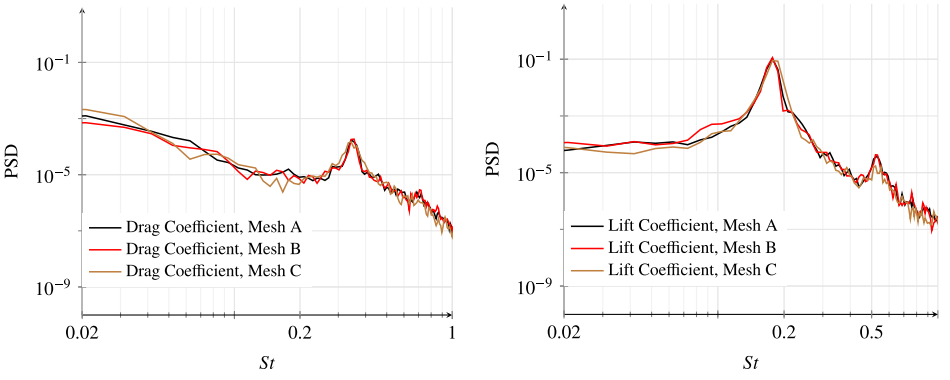

a) PSD of drag coefficient **b) PSD of lift coefficient**

Fig. 8 PSD of drag and lift coefficient over the rod.

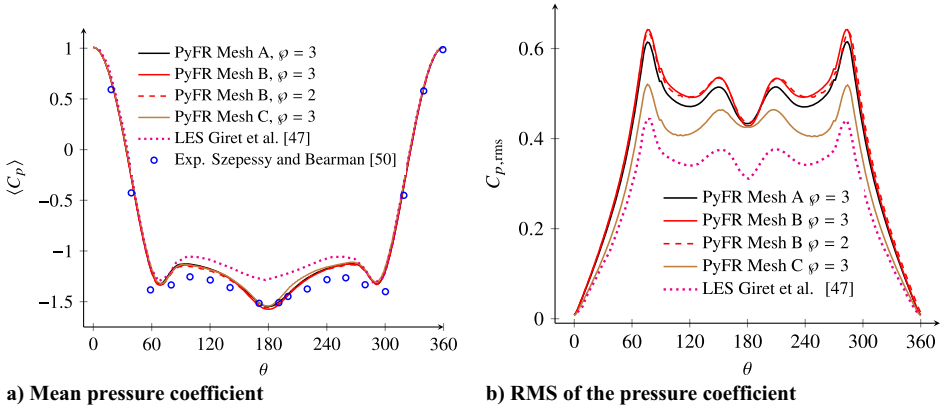

a) Mean pressure coefficient **b) RMS of the pressure coefficient**

Fig. 9 Average and rms of the pressure coefficient over the rod surface.

with the experiment of Ref. [50]. In the range of $\theta = 120$ deg to 240 deg, PyFR predictions show better agreement with the experimental results than with the LES data [47]. Meshes A and B share the same spanwise extent and a close agreement between meshes A and B indicates that increasing the spanwise resolution from 56 to 112 points has a negligible influence on the mean pressure distribution, demonstrating spanwise grid convergence for this quantity. Mesh C, which increases the spanwise domain length to 0.7 exhibits a slight reduction in suction in the range $\theta = 180$ deg to $\theta = 240$ deg. Overall, there is a good agreement between PyFR results and the experimental results of Ref. [50]. Figure 9b shows the variation of the root mean squared pressure coefficient $C_{p,\mathrm{rms}}$ over the rod for meshes A, B, and C. Meshes A and B show similar variation of rms pressure coefficient, although mesh B predicts slightly higher values of $C_{p,\mathrm{rms}}$. Increasing the spanwise domain length in mesh C results in a noticeable reduction in $C_{p,\mathrm{rms}}$ from

$\theta = 70$ deg to $\theta = 310$ deg. The reduced $C_{p,\text{rms}}$ levels observed for mesh C are attributed to decreased spanwise coherence and increased three-dimensionality enabled by the longer spanwise domain [53]. PyFR $\wp = 2$ and $\wp = 3$ results show similar variation in rms pressure coefficient for mesh B, indicating $\wp$-convergence. LES results of Ref. [47] predict a consistently lower amplitude than PyFR simulations. The discrepancy in magnitude between the current PyFR results and the reference LES is likely due to the different turbulence-modeling strategies. The LES uses an explicit subgrid-scale model and a lower-order discretization, which introduce additional dissipation and partially attenuate the small-scale turbulent pressure fluctuations at the rod surface. In contrast, the high-order FR–ILES approach used here exhibits much lower numerical dissipation, allowing a wider range of turbulent scales to be sustained and leading to higher $C_{p,\text{rms}}$ levels.

The comparison of the mean and rms pressure coefficient over the airfoil is shown in Fig. 10. In Fig. 10a, the mean pressure coefficient $\langle C_p \rangle$ from PyFR simulations is compared against LES data of Giret et al. [47] and experimental data of Jacob et al. [21]. Overall, all three PyFR meshes show good agreement with the LES data across most of the chord. Minor discrepancies are observed near the trailing edge, where differences between the PyFR results and LES results become more pronounced. Among the three configurations, mesh C exhibits the closest agreement with both the LES and experimental data in the trailing-edge region. The close agreement between meshes A and B indicates that increasing the spanwise resolution alone has a limited impact on $\langle C_p \rangle$, whereas extending the spanwise domain length has a more noticeable influence on the trailing-edge pressure levels. A consistent discrepancy is observed between all numerical results and the experimental data, which may be attributed to the curvature discontinuity in the mockup leading edge region as discussed in Ref. [47]. Figure 10b shows the distribution of the rms coefficient of pressure $C_{p,\text{rms}}$ over the airfoil surface. The results indicate a strong dependence on the spanwise domain size in the leading-edge region ($x/C < 0.4$). Both meshes A and B exhibit a high-intensity fluctuation peak near the leading edge ($C_{p,\text{rms}} = 2.3$). However, increasing the spanwise extent (mesh C) while maintaining the same spanwise grid density as mesh A results in a significant attenuation of this peak to 1.5. This suggests that the narrower domain may be artificially enforcing spanwise correlation or constraining large-scale structures impinging on the leading edge of the airfoil. Conversely, the solution appears to be relatively insensitive to grid refinement. Comparing mesh A and B shows negligible differences in the $C_{p,\text{rms}}$ profiles, indicating that the spanwise resolution of mesh A is sufficient to capture the relevant turbulent scales. Similarly, increasing the polynomial order from $\wp = 2$ to $\wp = 3$ on mesh B yields only minor variations in $C_{p,\text{rms}}$. In comparison to the LES reference data by Giret et al. [47], the present high-order FR results generally predict higher fluctuation levels for $x/C < 0.4$. The elevated rms values of pressure coefficient for $x/C < 0.4$ compared to the LES reference are attributed to higher numerical dissipation and different turbulence modeling strategies.

Figure 11 shows the spanwise averaged skin friction coefficient over the surface of the rod for meshes A, B, and C. Skin friction coefficient C_f drops to zero at an angle of 93 deg, indicating flow separation at $\theta = 93$ deg, which is within 5% of the literature value of 86 deg [47]. Although the peak $\langle C_f \rangle$ values are underpredicted in both PyFR results, it is important to note that the results in Ref. [54] correspond to the flow around an isolated rod at a relatively higher Reynolds number $R_e = 1 \times 10^{-5}$. In contrast to the fluctuating pressure statistics, the mean skin friction profiles exhibit negligible sensitivity to both grid resolution and spanwise domain size. The results for meshes A, B, and C are virtually indistinguishable. This indicates that the mean boundary-layer development and the primary separation location are well resolved and are not strongly influenced by the spanwise domain length or spanwise resolution. The convergence of all three meshes confirms that the near-wall resolution is sufficient to capture the viscous sublayer physics. Additionally, $\wp$-convergence was confirmed on mesh B as increasing the polynomial order from 2 to 3 yielded no significant variation in the C_f distribution. Because we have established the solution is $\wp$-converged, we only present results for $\wp = 3$ henceforth.

Figure 12 shows the average values of the x-velocity U and rms value of the x-velocity fluctuations U_{rms} at two different locations, namely, near the airfoil leading edge and wake of the airfoil which correspond to points P5 and P6 in Fig. 6. At $x/C = -0.25$, the mean velocity profiles exhibit a symmetric wake deficit. Mesh C predicts a slightly lower wake deficit when compared to meshes A and B. All three meshes accurately capture the wake width and show good agreement with the reference data of Ref. [12]. The turbulent

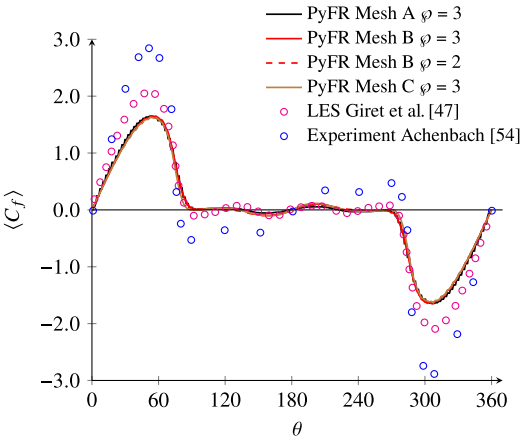

Fig. 11 Comparison of the mean skin friction $\langle C_f \rangle$ coefficient over the rod surface.

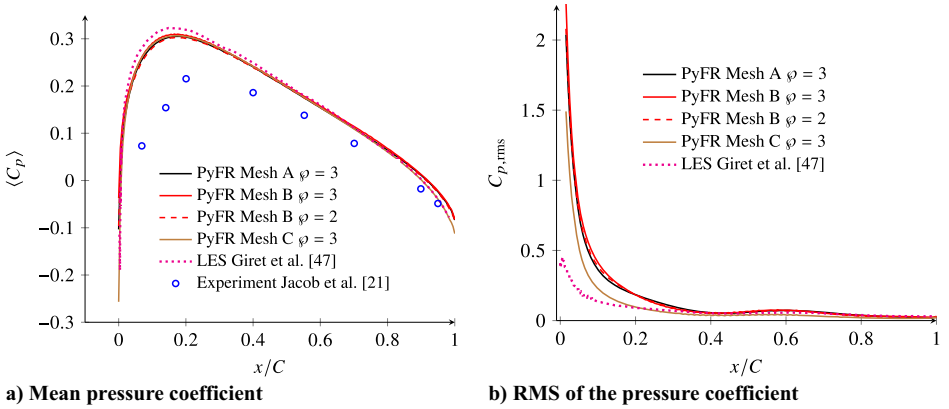

a) Mean pressure coefficient **b) RMS of the pressure coefficient**

Fig. 10 Average and rms of the pressure coefficient over the airfoil surface.

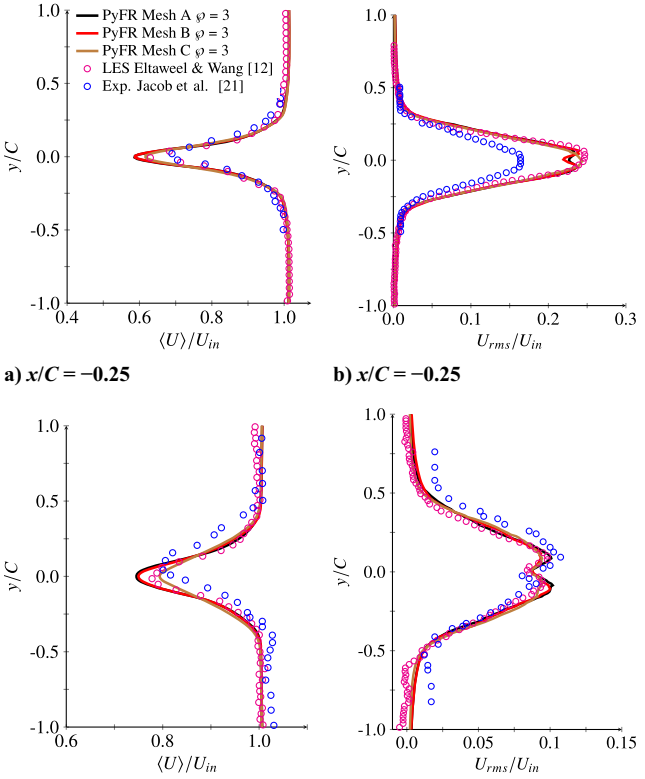

a) $x/C = -0.25$ **b)** $x/C = -0.25$

c) $x/C = 2$ **d)** $x/C = 2$

Fig. 12 Comparison of the mean and rms velocity profiles with experiment and reference LES in the wake of airfoil and aside the airfoil.

fluctuation profile (Fig. 12b) shows sensitivity to spanwise domain length. The narrower spanwise domain simulations (meshes A and B) exhibit a distinct double-peak structure in the U_{rms} profile, while the wider domain simulation (mesh C) predicts a single peak which indicates enhanced mixing between the shear layers [55]. The single-peak profile of mesh C aligns closely with the reference LES data [12]. The underprediction of U_{rms} in the experimental results at $x/C = 0.25$ can be attributed to hot-wire measurements, which can be as high as 30%. At $x/C = 2$, the wider domain mesh C predicts a shallower velocity deficit $\langle U \rangle / U_{\text{in}} = 0.8$ compared to the narrower domains ($\langle U \rangle / U_{\text{in}} = 0.74$) meshes A and B. This faster wake recovery indicates enhanced momentum diffusion due to stronger three-dimensional turbulence. The turbulence fluctuation velocity profile (Fig. 12d) in the airfoil wake predicts similar variation across all three meshes A, B, and C. Across all four subplots, the results for meshes A and B are virtually indistinguishable. This overlap confirms that the solution is strictly grid converged with respect to spanwise resolution. The discrepancies observed between the PyFR results, and the reference data are therefore isolated to spanwise domain confinement effects.

Figure 13 shows the energy spectra of streamwise velocity fluctuations at four locations, two in the rod wake and two on top of the airfoil. Figure 13a shows the energy spectra in the rod wake at $x/C = -0.87$ and $y/d = 0.05$ (P1 in Fig. 6). All three meshes A, B, and C predict the same peak frequency $St = 0.18$ corresponding to the fundamental shedding frequency of the cylinder lift fluctuations. Meshes B and C predict slightly higher amplitude levels in the low-frequency range ($St < 0.07$). Figure 13b shows the energy spectra along the rod axis at $x/C = -0.87$ and $y/d = 0.0$ (P2 in Fig. 6). The peak frequency at this point as predicted by PyFR is twice the fundamental shedding frequency. Because the point is along the rod axis, the vortex shedding from the top and bottom of the cylinder equally excites this point, and the peak frequency corresponds to the

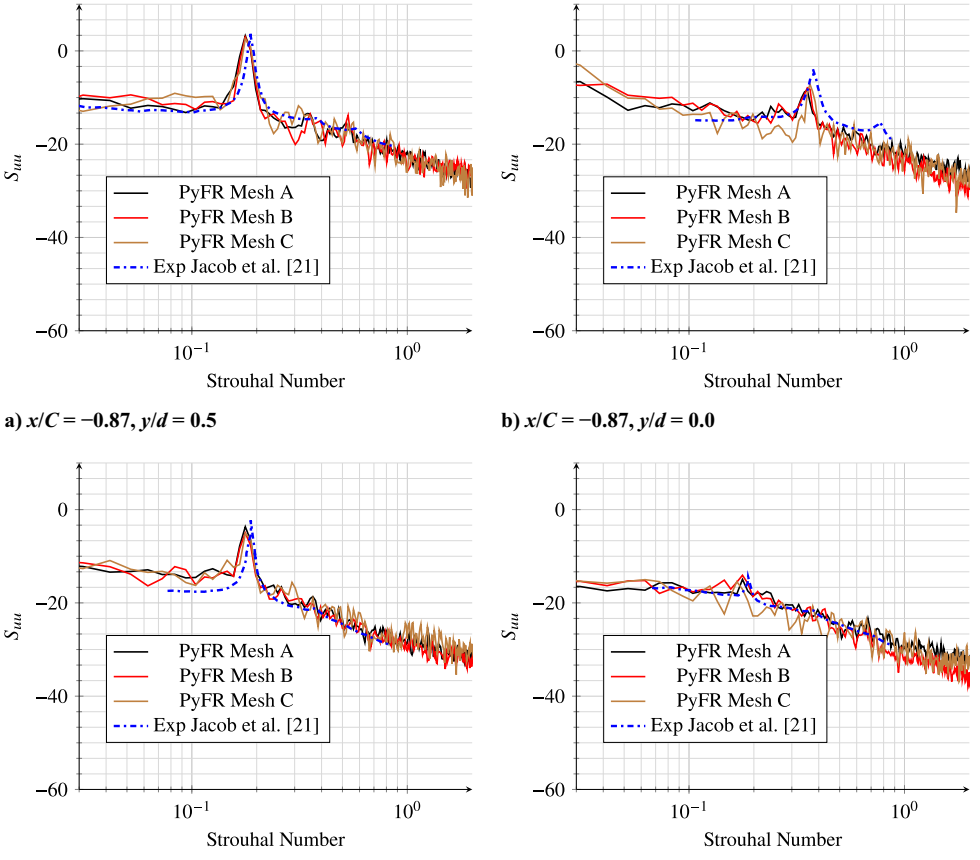

a) $x/C = -0.87$, $y/d = 0.5$ **b)** $x/C = -0.87$, $y/d = 0.0$

c) $x/C = 0.25$, $y/d = 0.8$ **d)** $x/C = 0.25$, $y/d = 1.6$

Fig. 13 Streamwise velocity energy spectra as a function of frequency at four locations.

drag fluctuations from the cylinder. Similar to P1, meshes B and C predict higher energy levels at very low frequencies ($St < 0.07$), while mesh C exhibits comparatively lower amplitudes in the intermediate range ($0.07 < St < 0.18$). Figures 13c and 13d show the energy spectra of streamwise velocity fluctuations on top of the airfoil at points P3 and P4 (Fig. 6), respectively. As we move away from the airfoil in the positive y direction, the intensity of turbulence decreases, which can be corroborated by the relatively lower peak levels seen in Fig. 13d. The peak frequency at both these points is equal to the fundamental shedding frequency of $St = 0.18$. At point P3 (Fig. 13c), all three meshes predict the same peak Strouhal number. At point P4, mesh C slightly underpredicts the peak frequency as seen in Fig. 13d.

Figure 14 presents the spanwise-averaged Power spectral density (PSD) of of wall-pressure fluctuations on the rod and airfoil for meshes A, B, and C. At the rod location $\theta = 80$ deg, measured clockwise from the forward stagnation point, a strong tonal component is observed at the fundamental vortex-shedding frequency corresponding to $St = 0.18$. A secondary peak is also evident at the first harmonic $St = 0.36$. The amplitudes of these peaks are higher in the PyFR simulations than in the LES data of Giret et al. [47], which can be due to the reduced numerical damping typically associated with high-order methods. Increasing the spanwise resolution at fixed spanwise length, from mesh A to mesh B, results in slightly higher peak amplitudes. Because the dominant contribution to $C_{p,\mathrm{rms}}$ arises from the fundamental peak, this behavior is consistent with the higher $C_{p,\mathrm{rms}}$ values reported for mesh B in Fig. 9. Increasing the spanwise extent to mesh C reduces the PSD levels and improves agreement with the LES spectrum in the range $0.15 < St < 0.4$, which is again consistent with the reduced $C_{p,\,\mathrm{rms}}$ observed in Fig. 9 for mesh C. At $\theta = 180$ deg, the dominant peak appears at twice the vortex-shedding frequency, reflecting the symmetric nature of the wake dynamics at this location. Mesh A predicts lower broadband levels than both the LES and the other PyFR simulations. Meshes A and B yield similar peak amplitudes, whereas mesh C predicts a reduced peak level consistent with the lower $C_{p,\mathrm{rms}}$ values reported for mesh C. Figure 14c shows the PSD at $x/C = 0.2$ on the airfoil surface. A clear tonal peak is present at the fundamental shedding frequency together with a weaker peak at first harmonic. Meshes A and B predict nearly identical spectral levels for $St < 0.5$, while mesh C again exhibits lower broadband level as well as peak levels.

B. Far-Field Acoustics Results

The FWH results are obtained for the three meshes A, B, and C for a nondimensional period $\tilde{t}$ of 100 units, where time is nondimensionalized based on airfoil chord. The FWH follows the Welch's method of periodograms [44] where the time period is divided into 10 windows each with a length of 10 nondimensional time units. The far-field acoustics are computed for each period and averaged with the others with a 50% shift in window length. The far-field acoustics are computed using two FWH surfaces, a solid surface that consists of the rod and airfoil walls and a porous surface as shown in Fig. 15. The porous surface takes a c-like shape and starts from $0.3C$ in front of the rod and up to $4C$ behind the airfoil as shown. This porous surface is chosen to enclose all the relevant turbulent structures in the near-field region.

The results of the PSD using the FWH solver computed for three far-field observers are presented in Fig. 16 for three meshes A, B, and C using a solid and a porous FWH surface. The three observers are located at a distance of $18.5C$ and angles of $\theta = 60$ deg, 90 deg

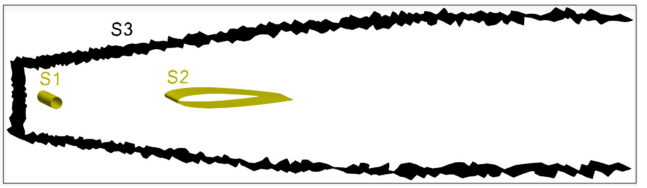

Fig. 15 FWH and solid and porous surface geometries. Solid surfaces are denoted S1 and S2, and the porous surface is S3.

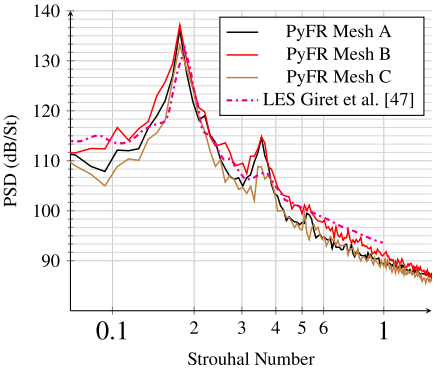

a) Rod $\theta = 80^\circ$

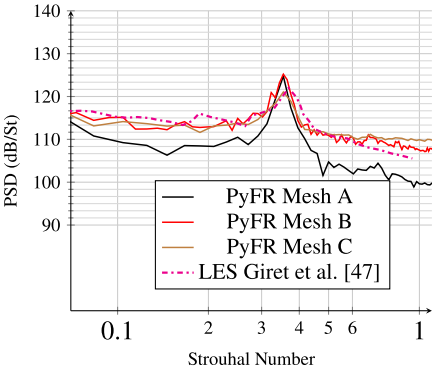

b) Rod $\theta = 180^\circ$

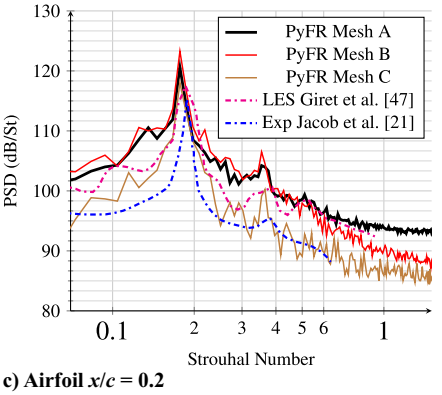

c) Airfoil $x/c = 0.2$

Fig. 14 Power spectral density over the rod and airfoil surface.

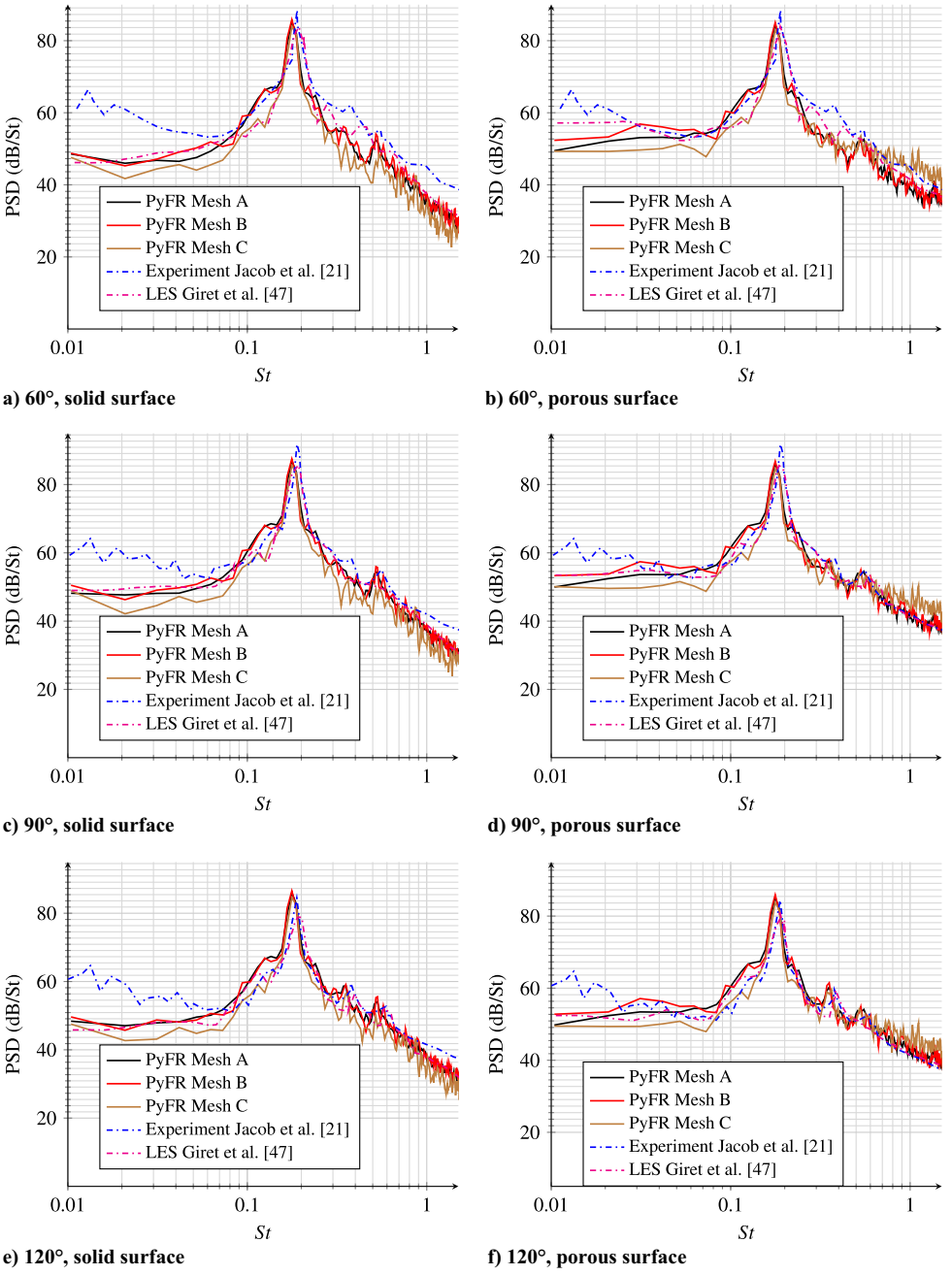

Fig. 16 Comparison of far-field acoustics at a distance $R = 18.5C$ measured from half-chord and $\theta = 60$ deg, 90 deg, 120 deg measured from the airfoil T.E (trailing edge).

and 120 deg (measured counterclockwise) with the origin at half the airfoil chord. At $\theta = 60$ deg, all meshes predict the same dominant tonal frequency at $St = 0.18$. The second harmonic associated with the rod–airfoil lift fluctuations is also captured by all three meshes. For the solid surface, meshes A and B exhibit very similar broadband PSD trends, whereas mesh C produces slightly lower broadband levels. For the porous FWH surface at this observer, mesh C again predicts reduced broadband levels for $St < 0.15$, while elevated levels appear at higher frequencies above $St > 0.7$. For both surfaces, mesh B predicts higher peak levels than the LES data, whereas meshes A and C predict similar peak levels to the LES data. The second observer at $\theta = 90$ deg again predicts the same peak frequency of $St = 0.18$ for all three meshes. Mesh B predicts elevated peak levels compared to the LES data for both the solid and porous FWH surfaces. Meshes A and C predict similar peak levels as the LES data for the porous surface, while being slightly above the LES peak levels for the solid surface. For the third observer at $\theta = 120$ deg, all meshes capture the dominant frequency as well as the first and second harmonics for both FWH surfaces. All three PyFR meshes predict higher peak levels compared to both LES and experimental data at this observer location.

Mesh B predicts the highest tonal peak levels for both the solid and porous FWH surfaces at all observer locations, whereas meshes A and C yield similar peak amplitudes. For all the observers, mesh C underpredicts broadband levels for $St < 0.15$ for the porous surface, while elevated broadband levels are seen for high frequencies at $St > 0.7$. For the solid surface, mesh C underpredicts the broadband levels in general for all three observers. The reduced PSD levels predicted by mesh C are consistent with the lower rms pressure coefficients observed over both the rod and the airfoil surfaces in Figs. 9 and 10. The broadband levels below $St = 0.07$ are underpredicted by PyFR at all locations and can be attributed to the background noise in the experiment as discussed in Ref. [47]. A Strouhal number of $St = 0.18$ is predicted by PyFR, which is about

5% lower than the experimental value of 0.19. However, it is worth noting that the rod and airfoil axis are misaligned in the experiment creating a 2 deg angle of attack for the airfoil. This could result in a difference in the Strouhal number.

Figure 17 illustrates the individual contributions of the rod and airfoil noise to the solid FWH surface at $\theta = 45$ deg, 90, 135, and 180 deg for mesh B. The rod, airfoil, and combined rod–airfoil noise predict the same peak frequency of $St = 0.18$. At $\theta = 45$ deg, airfoil contribution dominates the total noise for frequencies up to $St = 0.5$, with the peak airfoil noise at $St = 0.18$ measuring approximately 3.5 dB below the combined rod–airfoil signal. Below $St = 0.5$, the airfoil and rod–airfoil spectra are nearly identical, whereas for higher frequencies ($St > 0.5$), the rod contribution becomes more significant. Combined rod–airfoil noise and rod noise shows additional prominent peaks at the first and second harmonics, which correspond to the drag and lift fluctuations, respectively. At $\theta = 90$ deg, the airfoil remains the predominant source up to the second harmonic of $St = 0.54$. Beyond this point, rod-generated noise dominates the total emission. Rod noise shows a prominent peak at second harmonic, which corresponds to lift fluctuations. Because $\theta = 90$ deg is very close to the separation angle, the fluctuations at this point are dominated by the periodic vortex shedding. At $\theta = 135$ deg, the rod–airfoil noise exceeds both individual noise sources at peak frequency, indicating constructive interference between the two components. The peak frequency as well as the first and second harmonics are clearly visible in the power spectral density of rod and rod–airfoil noise. For observers at $\theta = 45$ deg, 90 deg and 135 deg, broadband levels of rod–airfoil combined and airfoil are nearly identical for $St < 0.5$, and the airfoil noise contribution to the total noise is higher than the rod noise in the range $St < 0.5$. At $\theta = 180$ deg, the peak frequency corresponds to the first harmonic of $St = 0.36$ associated with cylinder drag fluctuations, which is also observed in Fig. 14b. Here, the rod is the primary noise source, and constructive interference with the airfoil noise leads to an elevated total noise level. The peak frequency of $St = 0.18$ and second harmonic corresponding to the lift fluctuations are completely absent at this angle.

Figure 18 presents the directivity patterns of the airfoil, rod, and combined rod–airfoil configuration at Strouhal numbers $St = 0.18$ and 0.36, computed using the solid FWH surface. These are compared against LES results from Eltaweel and Wang [12]. At $St = 0.18$, the rod–airfoil configuration exhibits a dipolelike directivity. The PyFR results suggest that the airfoil contributes more significantly to the overall noise than the rod. This trend is also observed in the LES results for $\theta < 120$ deg, whereas beyond 120 deg, rod noise dominates in the LES data. For PyFR simulations, the sound pressure level of the rod–airfoil configuration exceeds that of the individual components across all angles. The peak levels predicted by PyFR and LES data for the combined noise are similar and equal to 95 dB at $\theta = 90$ deg. In general, PyFR predicts higher noise levels compared to LES data of Eltaweel and Wang at this frequency. Figure 18b shows the directivity at the first harmonic ($St = 0.36$). Here, the airfoil dominates the overall noise between 60 deg $< \theta <$ 150 deg. Rod contribution exceeds the airfoil contribution for $\theta > 150$ deg, whereas PyFR predicts equal contribution of rod and airfoil for $\theta < 60$ deg. Airfoil contribution to the overall noise is higher in the LES data of Eltaweel and Wang. The LES results of Eltaweel and Wang also show an additional dip in the rod PSD levels between $\theta = 85$ deg and $\theta = 95$ deg. A similar feature is also observed in the PyFR results, although the magnitude of the dip is less pronounced. The combined noise predicted by the LES data is higher than the PyFR noise in the range 45 deg $< \theta <$ 120 deg, whereas PyFR combined noise exceeds the LES levels for $\theta > 120$ deg and $\theta < 45$ deg. Both PyFR and LES predict that the combined rod–airfoil configuration produces higher noise levels than those generated by the rod and airfoil individually. Figure 18c displays the overall sound pressure level directivity for the rod–airfoil setup. It shows a dipolar distribution, similar to Fig. 18a. Constructive interference is evident at all angles, and airfoil noise consistently dominates over rod noise.

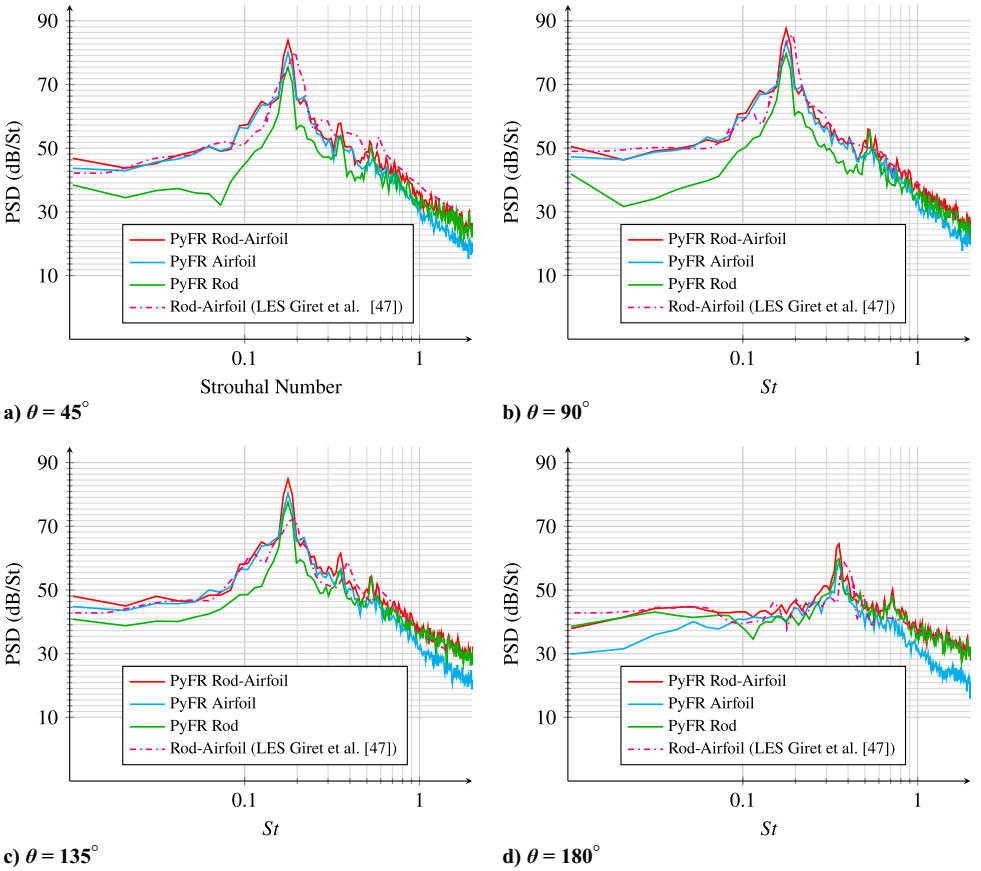

Fig. 17 Comparison of rod and airfoil contributions to the power spectral density of the solid FWH surface.

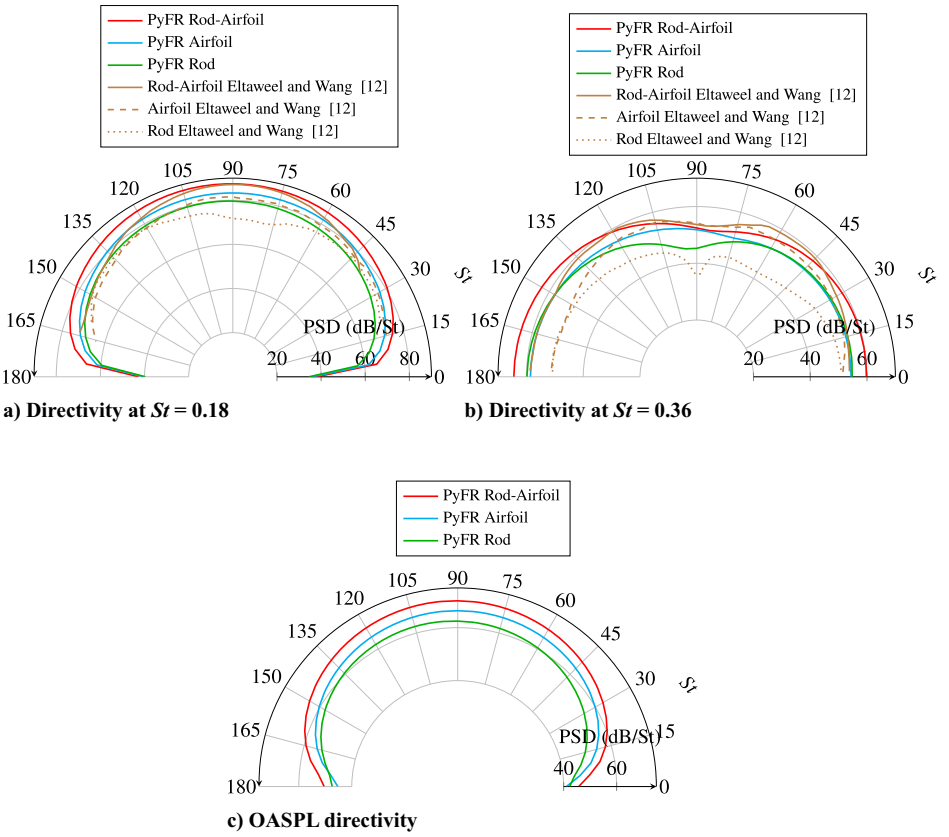

a) Directivity at $St = 0.18$ b) Directivity at $St = 0.36$

c) OASPL directivity

Fig. 18 Directivity plots at different Strouhal numbers and overall sound pressure level.

V. Conclusions

In this paper, we presented aerodynamic and acoustic results for the airfoil–rod benchmark case using a hybrid LES–FWH approach based on the high-order FR scheme with polynomial orders up to $\wp = 3$. A systematic mesh-sensitivity analysis was conducted using three meshes (A, B, and C) to assess the impact of spanwise resolution N_z and domain extent L_z on near-field statistics and far-field acoustics. Although mean statistics such as pressure and skin-friction coefficients showed excellent agreement with experimental data across all meshes, second-order statistics revealed a distinct sensitivity to domain size. Extending the spanwise length (mesh C) had a more significant impact than increasing resolution alone, resulting in improved predictions for pressure fluctuations, wake deficits, and broadband spectral levels. Despite these variations in magnitude, the fundamental spectral features remained robust. Notably, all three PyFR meshes converged to a Strouhal number St of 0.18. The far-field acoustic results obtained via both solid and porous FWH surfaces showed good consistency with each other and with literature benchmarks. Collectively, these findings confirm that the results are grid converged and that the ILES of the airfoil–rod benchmark case was successfully executed using the higher-order FR scheme.

Detailed analysis of the noise generation mechanisms revealed that the airfoil contribution to the overall sound pressure level generally exceeds that of the rod, except at very high frequencies, with constructive interferences leading to higher overall levels. Directivity analysis indicated a dipolar pattern for both the fundamental frequency and overall sound pressure level. The present results demonstrate that ILES can reproduce both the tonal and broadband components of the rod–airfoil noise with good fidelity, offering accuracy that is comparable to conventional LES while avoiding the complexity of explicit subgrid-scale modeling. This makes implicit LES an attractive and computationally efficient alternative for aeroacoustic simulations, particularly when combined with high-order spatial discretization. Although the present study employs explicit time integration, future developments will focus on implicit time-stepping strategies to reduce the overall computational cost while retaining the predictive capability demonstrated here.

Appendix A

To validate the current numerical framework for aeroacoustic prediction, a benchmark compressible flow simulation was performed for flow past a circular cylinder at a $R_{e,D}$ of 10,000 and a Mach number of 0.2. The simulations are run at a polynomial order $\wp = 2$. This flow regime is characterized by a laminar boundary-layer separation with transition to turbulence occurring in the separated shear layers. Figure A1 shows a close-up view of the mesh for flow over the cylinder.The computational domain extends $80D$ downstream of the cylinder and πD in the spanwise direction with periodic boundary conditions. Further details about the flow

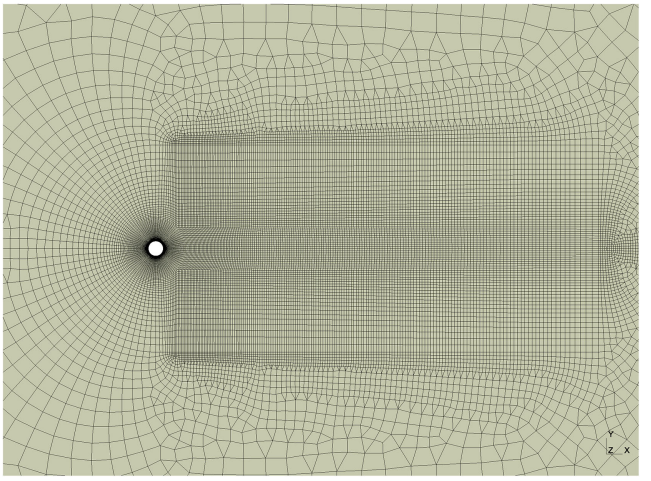

Fig. A1 Mesh for flow over a cylinder $Re = 10{,}000$.

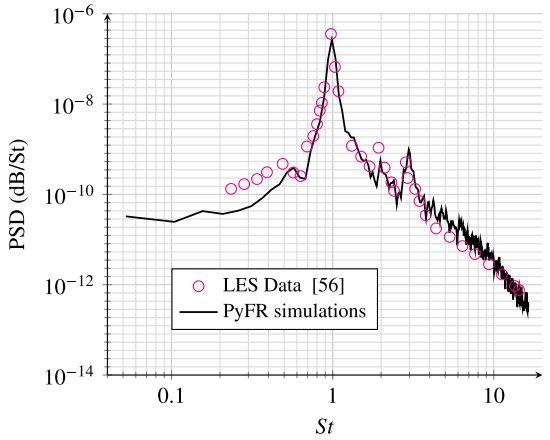

Fig. A2 Comparison of PSD for flow over a cylinder.

configuration can be found in Ref. [56]. The computed acoustic spectra are compared against the high-fidelity validation data provided by Khalighi et al. [56] for a far-field observer located at $(1.2D, 16.2D)$ in the midspan plane. The simulations are run for 50 shedding cycles, and the Welch method [44] is used to obtain the acoustic spectrum. As shown in Fig. A2, the current FWH implementation provides excellent agreement with the LES results. The primary vortex shedding tone is accurately captured at a Strouhal number of 0.19 ± 0.005, which is within 1% of the LES value of 0.192. Additionally, PyFR accurately predicts the peak amplitude of 5×10^{-7}. At low Strouhal numbers, the PyFR simulation underpredicts the spectral levels relative to the LES data. This discrepancy likely reflects sensitivity to numerical resolution and sampling duration, which more strongly influences the low-frequency content. The reference LES results include the quadrupolar volume source term in the Ffowcs Williams–Hawkings formulation, whereas this contribution is neglected in the present study. This difference may partly contribute to the observed discrepancies.

Acknowledgments

R. B. M. and F. D. W. would like to acknowledge support by the Air Force Office of Scientific Research via grant number FA9550-23-1-0232 ("Next Generation High-Order Methods for Multi-Physics Multi-Scale Problems") under the direction of Dr. Fariba Fahroo.

References

[1] Lunter, M., and Dickson, N., "Overview of the Thirteenth Cycle of the Committee on Aviation Environmental Protection (CAEP/13)," *International Civil Aviation Organization*, 2025, https://www.icao.int/sites/default/files/sp-files/environmental-protection/Documents/EnvironmentReport-2010/2025/Envreport2025_8.pdf.

[2] Liu, J., Kailasanath, K., Ramamurti, R., Munday, D., Gutmark, E., and Lohner, R., "Large-Eddy Simulations of a Supersonic Jet and Its Near-Field Acoustic Properties," *AIAA Journal*, Vol. 47, No. 8, 2009, pp. 1849–1865. https://doi.org/10.2514/1.43281

[3] Mendez, S., Shoeybi, M., Lele, S. K., and Moin, P., "On the Use of the Ffowcs Williams–Hawkings Equation to Predict Far-Field Jet Noise from Large-Eddy Simulations," *International Journal of Aeroacoustics*, Vol. 12, No. 1/2, 2013, pp. 1–20. https://doi.org/10.1260/1475-472X.12.1-2.1

[4] Brès, G. A., Ham, F. E., Nichols, J. W., and Lele, S. K., "Unstructured Large-Eddy Simulations of Supersonic Jets," *AIAA Journal*, Vol. 55, No. 4, 2017, pp. 1164–1184. https://doi.org/10.2514/1.J055084

[5] Liu, J., Corrigan, A. T., Kailasanath, K., Ramamurti, R., and Gutmark, E. J., "Helical Screech Tone Generation in an Overexpanded Jet," *23rd AIAA/CEAS Aeroacoustics Conference*, AIAA Paper 2017-3208, 2017. https://doi.org/10.2514/6.2017-3208

[6] Lyrintzis, A. S., and Coderoni, M., "The Use of Large Eddy Simulations in Jet Aeroacoustics," *AIAA Scitech 2019 Forum*, AIAA Paper 2019-0633, 2019. https://doi.org/10.2514/6.2019-0633

[7] Casalino, D., Jacob, M., and Roger, M., "Prediction of Rod-Airfoil Interaction Noise Using the Ffowcs-Williams–Hawkings Analogy," *AIAA Journal*, Vol. 41, No. 2, 2003, pp. 182–191. https://doi.org/10.2514/2.1959

[8] Greschner, B., Thiele, F., Jacob, M. C., and Casalino, D., "Prediction of Sound Generated by a Rod–Airfoil Configuration Using EASM DES and the Generalised Lighthill/FW-H Analogy," *Computers & Fluids*, Vol. 37, No. 4, 2008, pp. 402–413. https://doi.org/10.1016/j.compfluid.2007.02.013

[9] Caraeni, M., Aybay, O., and Holst, S., "Tandem Cylinder and Idealized Side Mirror Far-Field Noise Predictions Using DES and an Efficient Implementation of FW-H Equation," *17th AIAA/CEAS Aeroacoustics Conference (32nd AIAA Aeroacoustics Conference)*, AIAA Paper 2011-2843, 2011. https://doi.org/10.2514/6.2011-2843

[10] Zhang, Y., Chen, H., Wang, K., and Wang, M., "Aeroacoustic Prediction of a Multi-Element Airfoil Using Wall-Modeled Large-Eddy Simulation," *AIAA Journal*, Vol. 55, No. 12, 2017, pp. 4219–4233. https://doi.org/10.2514/1.J055853

[11] Boudet, J., Casalino, D., Jacob, M., and Ferrand, P., "Prediction of Sound Radiated by a Rod Using Large Eddy Simulation," *9th AIAA/CEAS Aeroacoustics Conference and Exhibit*, AIAA Paper 2003-3217, 2003. https://doi.org/10.2514/6.2003-3217

[12] Eltaweel, A., and Wang, M., "Numerical Simulation of Broadband Noise from Airfoil-Wake Interaction," *17th AIAA/CEAS Aeroacoustics Conference (32nd AIAA Aeroacoustics Conference)*, AIAA Paper 2011-2802, 2011. https://doi.org/10.2514/6.2011-2802

[13] Berland, J., Lafon, P., Crouzet, F., Daude, F., and Bailly, C., "Numerical Insight into Sound Sources of a Rod-Airfoil Flow Configuration Using Direct Noise Calculation," *16th AIAA/CEAS Aeroacoustics Conference*, AIAA Paper 2010-3705, 2010. https://doi.org/10.2514/6.2010-3705

[14] Peth, S., Seo, J., Jacob, M., and Thiele, F., "Computation of Aerodynamic Noise from Rod Wake-Airfoil Interactions," *European Conference on Computational Fluid Dynamics*, 2006, https://repository.tudelft.nl/file/File_a4228a8e-1456-4d57-b49b-4285a9c02ebe?preview=1.

[15] Vincent, P., Castonguay, P., and Jameson, A., "Insights from Von Neumann Analysis of High-Order Flux Reconstruction Schemes," *Journal of Computational Physics*, Vol. 230, No. 22, 2011, pp. 8134–8154. https://doi.org/10.1016/j.jcp.2011.07.013

[16] Hesthaven, J. S., and Warburton, T., *Nodal Discontinuous Galerkin Methods: Algorithms, Analysis, and Applications*, Springer, Berlin, 2011. https://doi.org/10.1007/978-0-387-72067-8

[17] Huynh, H. T., "A Flux Reconstruction Approach to High-Order Schemes Including Discontinuous Galerkin Methods," *18th AIAA Computational Fluid Dynamics Conference*, AIAA Paper 2007-4079, 2007. https://doi.org/10.2514/6.2007-4079

[18] Alhawwary, M. A., and Wang, Z. J., "Implementation of a FWH Approach in a High-Order LES Tool for Aeroacoustic Noise Predictions," *AIAA Scitech 2020 Forum*, AIAA Paper 2020-1724, 2020. https://doi.org/10.2514/6.2020-1724

[19] Lindblad, D., Sherwin, S., Cantwell, C., Lawrence, J., Proenca, A., and Moragues Ginard, M., "Aeroacoustic Analysis of a Subsonic Jet Using the Discontinuous Galerkin Method," *28th AIAA/CEAS Aeroacoustics 2022 Conference*, AIAA Paper 2022-2932, 2022. https://doi.org/10.2514/6.2022-2932

[20] Casalino, D., and Jacob, M., "Prediction of Aerodynamic Sound from Circular Rods via Spanwise Statistical Modelling," *Journal of Sound and Vibration*, Vol. 262, No. 4, 2003, pp. 815–844. https://doi.org/10.1016/S0022-460X(02)01136-7

[21] Jacob, M. C., Boudet, J., Casalino, D., and Michard, M., "A Rod-Airfoil Experiment as a Benchmark for Broadband Noise Modeling," *Theoretical and Computational Fluid Dynamics*, Vol. 19, No. 3, 2005, pp. 171–196. https://doi.org/10.1007/s00162-004-0108-6

[22] Witherden, F., Farrington, A., and Vincent, P., "PyFR: An Open Source Framework for Solving Advection–Diffusion Type Problems on Streaming Architectures Using the Flux Reconstruction Approach," *Computer Physics Communications*, Vol. 185, No. 11, 2014, pp. 3028–3040. https://doi.org/10.1016/j.cpc.2014.07.011

[23] Witherden, F., Vermeire, B., and Vincent, P., "Heterogeneous Computing on Mixed Unstructured Grids with PyFR," *Computers & Fluids*,

Vol. 120, Oct. 2015, pp. 173–186.
https://doi.org/10.1016/j.compfluid.2015.07.016
[24] Huynh, H. T., "A Flux Reconstruction Approach to High-Order Schemes Including Discontinuous Galerkin Methods," *18th AIAA Computational Fluid Dynamics Conference*, AIAA Paper 2007-4079, 2007. https://doi.org/10.2514/6.2007-4079
[25] Vincent, P. E., Castonguay, P., and Jameson, A., "A New Class of High-Order Energy Stable Flux Reconstruction Schemes," *Journal of Scientific Computing*, Vol. 47, No. 1, 2011, pp. 50–72.
https://doi.org/10.1007/s10915-010-9420-z
[26] Castonguay, P., Williams, D. M., Vincent, P. E., and Jameson, A., "Energy Stable Flux Reconstruction Schemes for Advection–Diffusion Problems," *Computer Methods in Applied Mechanics and Engineering*, Vol. 267, Oct. 2013, pp. 400–417.
https://doi.org/10.1016/j.cma.2013.08.012
[27] Gao, H., Wang, Z. J., and Huynh, H. T., "Differential Formulation of Discontinuous Galerkin and Related Methods for the Navier–Stokes Equations," *Communications in Computational Physics*, Vol. 13, No. 04, 2013, pp. 1013–1044.
https://doi.org/10.4208/cicp.020611.090312a
[28] Wang, Z., and Gao, H., "A Unifying Lifting Collocation Penalty Formulation Including the Discontinuous Galerkin, Spectral Volume/Difference Methods for Conservation Laws on Mixed Grids," *Journal of Computational Physics*, Vol. 228, No. 21, 2009, pp. 8161–8186.
https://doi.org/10.1016/j.jcp.2009.07.036
[29] Vermeire, B., and Vincent, P., "On the Properties of Energy Stable Flux Reconstruction Schemes for Implicit Large Eddy Simulation," *Journal of Computational Physics*, Vol. 327, Dec. 2016, pp. 368–388.
https://doi.org/10.1016/j.jcp.2016.09.034
[30] Wang, Z. J., Li, Y., Jia, F., Laskowski, G. M., Kopriva, J., Paliath, U., and Bhaskaran, R., "Towards Industrial Large Eddy Simulation Using the FR/CPR Method," *Computers & Fluids*, Vol. 156, Oct. 2017, pp. 579–589.
https://doi.org/10.1016/j.compfluid.2017.04.026
[31] Crabill, J., Witherden, F., and Jameson, A., "A Parallel Direct Cut Algorithm for High-Order Overset Methods with Application to a Spinning Golf Ball," *Journal of Computational Physics*, Vol. 374, Dec. 2018, pp. 692–723.
https://doi.org/10.1016/j.jcp.2018.05.036
[32] Alhawwary, M. A., and Wang, Z. J., "DNS and LES of the Flow over the T106C Turbine Using the High-Order FR/CPR Method," *AIAA Scitech 2020 Forum*, AIAA Paper 2020-1572, 2020.
https://doi.org/10.2514/6.2020-1572
[33] Iyer, A., Abe, Y., Vermeire, B., Bechlars, P., Baier, R., Jameson, A., Witherden, F., and Vincent, P., "High-Order Accurate Direct Numerical Simulation of Flow over a MTU-T161 Low Pressure Turbine Blade," *Computers & Fluids*, Vol. 226, Aug. 2021, Paper 104989.
https://doi.org/10.1016/j.compfluid.2021.104989
[34] Dzanic, T., Girimaji, S., and Witherden, F., "Partially-Averaged Navier–Stokes Simulations of Turbulence Within a High-Order Flux Reconstruction Framework," *Journal of Computational Physics*, Vol. 456, May 2022, Paper 110992.
https://doi.org/10.1016/j.jcp.2022.110992
[35] Rusanov, V., "The Calculation of the Interaction of Non-Stationary Shock Waves and Obstacles," *USSR Computational Mathematics and Mathematical Physics*, Vol. 1, No. 2, 1962, pp. 304–320.
https://doi.org/10.1016/0041-5553(62)90062-9
[36] Davis, S. F., "Simplified Second-Order Godunov-Type Methods," *SIAM Journal on Scientific and Statistical Computing*, Vol. 9, No. 3, 1988, pp. 445–473.
https://doi.org/10.1137/0909030
[37] Cockburn, B., and Shu, C.-W., "The Local Discontinuous Galerkin Method for Time-Dependent Convection-Diffusion Systems," *SIAM Journal on Numerical Analysis*, Vol. 35, No. 6, 1998, pp. 2440–2463.
https://doi.org/10.1137/S0036142997316712
[38] Kennedy, C. A., Carpenter, M. H., and Lewis, R., "Low-Storage, Explicit Runge–Kutta Schemes for the Compressible Navier–Stokes Equations," *Applied Numerical Mathematics*, Vol. 35, No. 3, 2000, pp. 177–219.
https://doi.org/10.1016/S0168-9274(99)00141-5
[39] Huynh, H. T., Wang, Z. J., and Vincent, P. E., "High-Order Methods for Computational Fluid Dynamics: A Brief Review of Compact Differential Formulations on Unstructured Grids," *Computers & Fluids*, Vol. 98, July 2014, pp. 209–220.
https://doi.org/10.1016/j.compfluid.2013.12.007
[40] Witherden, F., Vincent, P., and Jameson, A., "High-Order Flux Reconstruction Schemes," *Handbook of Numerical Analysis*, Vol. 17, Elsevier, New York, 2016, pp. 227–263.
https://doi.org/10.1016/bs.hna.2016.09.010
[41] Wozniak, B. D., Witherden, F. D., Russell, F. P., Vincent, P. E., and Kelly, P. H., "Gimmik—Generating Bespoke Matrix Multiplication Kernels for Accelerators: Application to High-Order Computational Fluid Dynamics," *Computer Physics Communications*, Vol. 202, May 2016, pp. 12–22.
https://doi.org/10.1016/j.cpc.2015.12.012
[42] Witherden, F. D., Vincent, P. E., Trojak, W., Abe, Y., Akbarzadeh, A., Akkurt, S., Alhawwary, M., Caros, L., Dzanic, T., Giangaspero, G., et al., "PyFR v2.0.3: Towards Industrial Adoption of Scale-Resolving Simulations," *Computer Physics Communications*, Vol. 311, June 2025, Paper 109567.
https://doi.org/10.1016/j.cpc.2025.109567
[43] Ghorbaniasl, G., and Lacor, C., "A Moving Medium Formulation for Prediction of Propeller Noise at Incidence," *Journal of Sound and Vibration*, Vol. 331, No. 1, 2012, pp. 117–137.
https://doi.org/10.1016/j.jsv.2011.08.018
[44] Welch, P., "The Use of Fast Fourier Transform for the Estimation of Power Spectra: A Method Based on Time Averaging over Short, Modified Periodograms," *IEEE Transactions on Audio and Electroacoustics*, Vol. 15, No. 2, 1967, pp. 70–73.
https://doi.org/10.1109/TAU.1967.1161901
[45] Boudet, J., Casalino, D., Jacob, M., and Ferrand, P., "Prediction of Broadband Noise: Airfoil in the Wake of a Rod," *42nd AIAA Aerospace Sciences Meeting and Exhibit*, AIAA Paper 2004-0852, 2004.
https://doi.org/10.2514/6.2004-852
[46] Eltaweel, A., Wang, M., Kim, D., Thomas, F. O., and Kozlov, A. V., "Numerical Investigation of Tandem-Cylinder Noise Reduction Using Plasma-Based Flow Control," *Journal of Fluid Mechanics*, Vol. 756, Oct. 2014, pp. 422–451.
https://doi.org/10.1017/jfm.2014.420
[47] Giret, J.-C., Sengissen, A., Moreau, S., Sanjosé, M., and Jouhaud, J.-C., "Noise Source Analysis of a Rod–Airfoil Configuration Using Unstructured Large-Eddy Simulation," *AIAA Journal*, Vol. 53, No. 4, 2015, pp. 1062–1077.
https://doi.org/10.2514/1.J053371
[48] Jin, Y., Liao, F., Cai, J., and Morris, P. J., "Investigation on Rod-Airfoil Noise with High-Order Cell-Centered Finite Difference Method and Acoustic Analogy," *Aerospace Science and Technology*, Vol. 102, July 2020, Paper 105851.
https://doi.org/10.1016/j.ast.2020.105851
[49] Karypis, G., and Kumar, V., "Metis: A Software Package for Partitioning Unstructured Graphs, Partitioning Meshes, and Computing Fill-Reducing Orderings of Sparse Matrices," Jan. 1997, https://conservancy.umn.edu/items/2f610239-590c-45c0-bcd6-321036aaad56.
[50] Szepessy, S., and Bearman, P. W., "Aspect Ratio and End Plate Effects on Vortex Shedding from a Circular Cylinder," *Journal of Fluid Mechanics*, Vol. 234, Jan. 1992, pp. 191–217.
https://doi.org/10.1017/S0022112092000752
[51] Schewe, G., "On the Force Fluctuations Acting on a Circular Cylinder in Crossflow from Subcritical up to Transcritical Reynolds Numbers," *Journal of Fluid Mechanics*, Vol. 133, Aug. 1983, pp. 265–285.
https://doi.org/10.1017/S0022112083001913
[52] Gerrard, J. H., "The Mechanics of the Formation Region of Vortices Behind Bluff Bodies," *Journal of Fluid Mechanics*, Vol. 25, No. 2, 1966, pp. 401–413.
https://doi.org/10.1017/S0022112066001721
[53] Chen, G., Zang, B., and Azarpeyvand, M., "The Effect of Spanwise Length on the Near-Field Dynamics of Flow Past a Cylinder Using Large-Eddy Simulation," *AIAA AVIATION 2021 Forum*, AIAA Paper 2021-2538, 2021.
https://doi.org/10.2514/6.2021-2538
[54] Achenbach, E., "Distribution of Local Pressure and Skin Friction Around a Circular Cylinder in Cross-Flow Up to Re = 5×106," *Journal of Fluid Mechanics*, Vol. 34, No. 4, 1968, pp. 625–639.
https://doi.org/10.1017/S0022112068002120
[55] Williamson, c., "Vortex Dynamics in the Cylinder Wake," *Annual Review of Fluid Mechanics*, Vol. 28, No. 1, 1996, pp. 477–539.
https://doi.org/10.1146/annurev.fl.28.010196.002401
[56] Khalighi, Y., Mani, A., Ham, F., and Moin, P., "Prediction of Sound Generated by Complex Flows at Low Mach Numbers," *AIAA Journal*, Vol. 48, No. 2, 2010, pp. 306–316.
https://doi.org/10.2514/1.42583

P. G. Tucker
Associate Editor